frontiers | Frontiers in Physics

TYPE Original Research
PUBLISHED 04 August 2023
DOI 10.3389/fphy.2023.1234054

Check for updates

OPEN ACCESS

EDITED BY
Li Li,
Harbin Institute of Technology, China

REVIEWED BY
Mingbo Pu,
Chinese Academy of Sciences (CAS), China
Hongzhan Liu,
South China Normal University, China

*CORRESPONDENCE
Qingli Zhou,
qlzhou@cnu.edu.cn

RECEIVED 03 June 2023
ACCEPTED 24 July 2023
PUBLISHED 04 August 2023

CITATION
Deng Y, Zhou Q, Zhang X, Zhang P, Liang W, Ning T, Shi Y and Zhang C (2023), Multi-state polarization switching and multifunction-integrated terahertz metadevice enabled by inverse resonance responses.
Front. Phys. 11:1234054.
doi: 10.3389/fphy.2023.1234054

COPYRIGHT
© 2023 Deng, Zhou, Zhang, Zhang, Liang, Ning, Shi and Zhang. This is an open-access article distributed under the terms of the Creative Commons Attribution License (CC BY). The use, distribution or reproduction in other forums is permitted, provided the original author(s) and the copyright owner(s) are credited and that the original publication in this journal is cited, in accordance with accepted academic practice. No use, distribution or reproduction is permitted which does not comply with these terms.

Multi-state polarization switching and multifunction-integrated terahertz metadevice enabled by inverse resonance responses

Yuwang Deng[1], Qingli Zhou[1]*, Xuteng Zhang[1], Pujing Zhang[1], Wanlin Liang[1], Tingyin Ning[2], Yulei Shi[1] and Cunlin Zhang[1]

[1]Beijing Advanced Innovation Center for Imaging Theory and Technology, Key Laboratory of Terahertz Optoelectronics, Ministry of Education, Department of Physics, Capital Normal University, Beijing, China, [2]Shandong Provincial Engineering and Technical Center of Light Manipulations & Shandong Provincial Key Laboratory of Optics and Photonic Device, School of Physics and Electronics, Shandong Normal University, Jinan, China

Dynamical control of terahertz metadevices and integration of versatile functions are highly desired due to increasing practical demands. Here, we propose a multifunctional photosensitive Si hybrid metastructure consisting of twisted split-ring resonator pairs that could empower multi-state polarization switching and object-recognized imaging. The theoretical and simulated results show that inverse complete modulation of cross-polarized components could be realized via tuning the conductivity of the Si-bridge. The calculated ellipticity indicates that our metadevices possess the ability to convert linearly polarized light into left-hand circular-polarized or right-hand circular-polarized waves, as well as left-hand circular-polarized or right-hand circular-polarized into linearly polarized states. Combined with these properties, mono-parameter amplitude imaging and amplitude-phase synergistic encryption imaging are accomplished. Our research provides a new strategy to develop reconfigurable and multifunctional components in the terahertz regime.

KEYWORDS

terahertz, metadevice, multi-state polarization switching, multifunction-integrated, resonance coupling

1 Introduction

Metasurfaces, as artificially designed structures with fascinating capabilities for manipulating light-matter interactions, have attracted much attention owing to their extraordinary properties not achievable in natural materials [1–4]. In the terahertz (THz) range, metasurfaces can achieve the effective regulation of optical characteristics, including amplitude, phase, frequency, and polarization [5–8]. Polarization is not only a degree of freedom in modulation of electromagnetic waves but also an ideal information carrier for imaging, sensing, communication, and spectroscopy systems [9–13]. Currently, single- or multi-layer wire-grid schemes [14, 15], chiral metasurfaces [16], all-dielectric metamaterials [17], and split-ring resonator (SRR) arrays [8, 18–20] are often used to fulfill polarization control of THz waves [21–26]. Herein, SRRs presented exotic spectral responses through geometric optimization, possessing simultaneously magnetic and electrical resonances as well as magnetoelectric coupling [27, 28]. These excellent performances lay the foundation for polarization investigations in SRR-based devices. In recent years, the

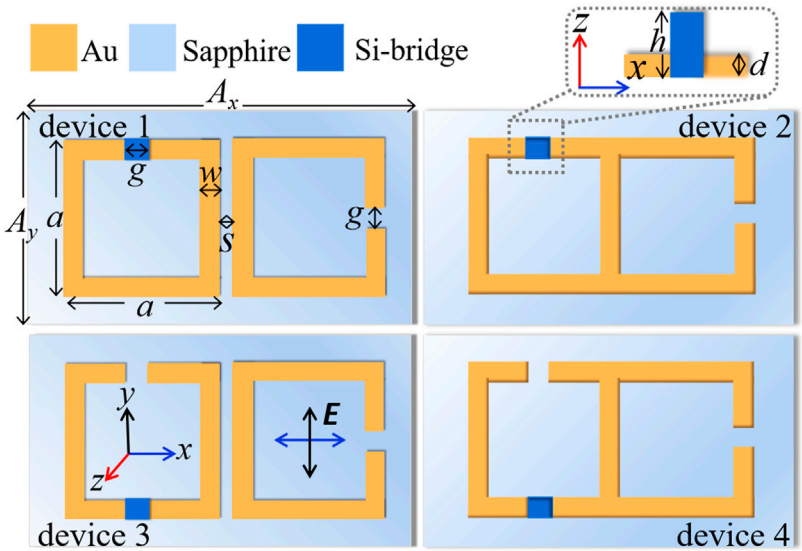

FIGURE 1
Schematic unit cells of the proposed hybrid metadevices from device 1 to device 4 with geometric parameters specified: A_x = 72 μm, A_y = 48 μm, w = 4 μm, g = 4 μm, d = 200 nm, h = 600 nm, and a the arm length of the SRR.

development of metadevices that can dynamically regulate optical behaviors has gradually earned intensive concerns due to the advantages of reconfigurability in various application fields. Integrating metasurfaces with dielectric tunable materials is a well-accepted approach to realize controllable THz wave polarization engineering [29–31]. For instance, a governable polarization rotator has been presented in a hybrid graphene metadevice via applying different bias voltages to adjust the Fermi energy of graphene [32]. The phase transition material has also been used to design the hybrid metastructure with broadband absorption and enhanced polarization conversion efficiency [33, 34]. In addition, it is reported that the active composite metasurfaces integrated with semiconductor Si and Ge can be utilized to implement ultrafast polarization switching [35, 36]. These excellent investigations mainly focus on converting the incident LP wave into its cross-polarized mode or a single circularly polarized light. However, there is a lack of studies on multifunctional and miniaturized metamaterials that involve the switching of multiple THz wave polarization states. In addition, traditional imaging based on polarization is mainly operated by using a single-parameter amplitude. The multi-parameter synergistic effect of amplitude and phase is more important in encryption imaging and information acquisition.

In this work, to achieve the switching of multiple polarization states of the THz wave and expand application scenarios, we theoretically and simulationally demonstrate the hybrid twisted SRR pair metadevices with cross-polarization conversion capacity and inverse reconfigurability. Using the photosensitive conductivity of the embedded Si-bridge, the dynamical and full modulation of the cross-polarized component is realized. The results exhibit that our metadevices are capable of converting LP light into LCP or RCP waves, as well as LCP or RCP into LP states. Moreover, the indirect amplitude-dependent imaging and direct amplitude–phase synergistic imaging can be achieved. The designed hybrid metadevices exhibit great advantages in the manipulation of polarization switching and provide a novel tactic for encryption imaging in the THz region.

2 Structure design and theory calculation

The unit cells of the designed hybrid metadevices, composed of twisted SRR pairs with the integration of a tunable photosensitive Si-bridge, are illustrated in Figure 1. The substrate is sapphire with a thickness of 500 μm and a dielectric permittivity of 11.7. The spacing s between two SRRs is 2 μm for device 1 and device 3 and 0 μm for device 2 and device 4, respectively. The Si-bridge, indicated by the blue area, is embedded in the 4 μm-wide gap. Based on these predefined settings, the finite-element simulation method is carried out using the commercial software COMSOL Multiphysics. A unit cell is selected as the simulation domain, and the periodic conditions are imposed on the surrounding boundaries. The top port in the air and the bottom port in the substrate are used for light excitation and output, respectively. Here, Au is considered a perfect electric conductor. An LP plane wave propagating along the z-direction is normally incident to the proposed metasurface. In the experiment, metastructures can be fabricated on a silicon-on-sapphire wafer composed of a 600 nm-thick intrinsic epitaxial Si layer formed on a sapphire substrate [6, 35, 37]. First, the patterning of the Si-bridge can be realized by a photolithography method combined with reactive ion etching. Next, the second-round photolithography, followed by deposition and lift-off steps, is carried out to define the periodic metallic surfaces aligned between patterned Si-bridges. After fabrication, the devices can be measured by using the optical pump terahertz-probe system [38].

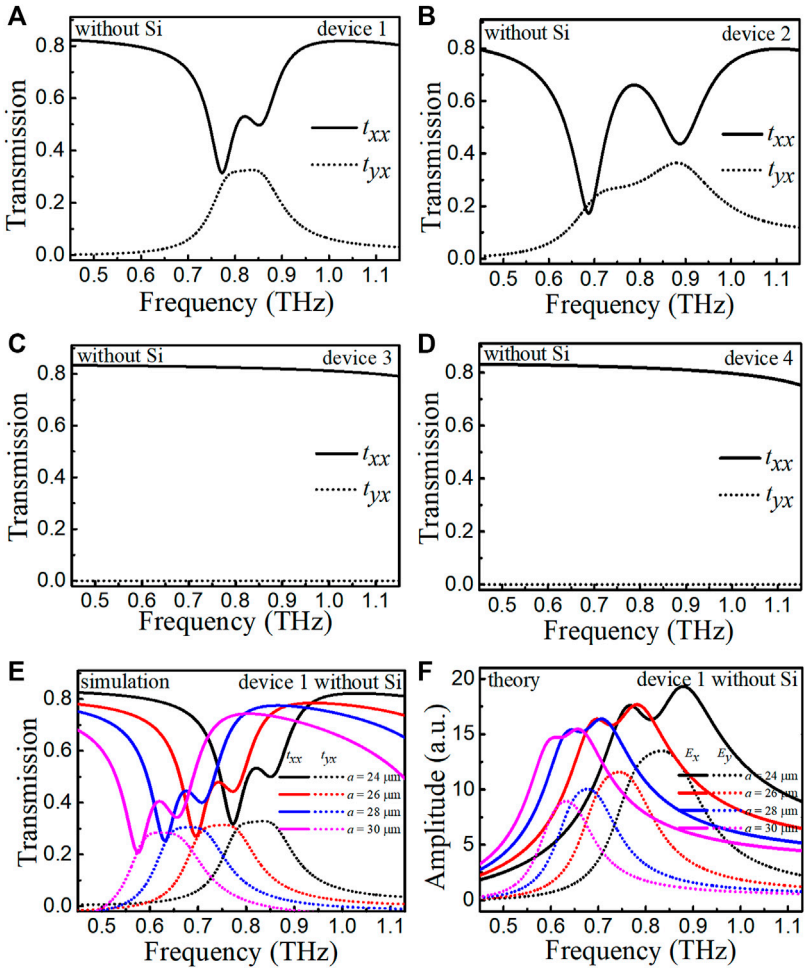

FIGURE 2
Simulated co- and cross-polarized transmission spectra of four hybrid metastructures without the Si-bridge for **(A)** device 1, **(B)** device 2, **(C)** device 3, and **(D)** device 4, respectively. **(E, F)** Simulated transmission curves and the corresponding theoretical amplitude spectra of E_x and E_y for device 1 with the increased a.

TABLE 1 Theoretical parameters used in the *RLC* model.

a (μm)	f_{SRR} (THz)	L (pH)	C (fF)	R (Ω)
24	0.809	48	0.80	37.65
26	0.733	54	0.88	38.09
28	0.670	60	0.95	38.54
30	0.619	65	1.00	39.10

To explore the polarization characteristics of twisted SRR pairs, we plot the simulated transmission spectra for hybrid structures without the Si-bridge in Figure 2. These curves represent co-polarized transmission t_{xx} and cross-polarized t_{yx} of metastructures (where a is fixed at 24 μm) with the incident field linearly polarized in the x-direction. The features of device 1 in Figure 2A indicate the emergence of considerable cross-polarized components and resonance splitting windows. Figure 2B shows the enhanced resonance splitting accompanied by a broad t_{yx} band of device 2. For device 3 and device 4, it is worth highlighting that the transmission curve of t_{xx} is a flat line with the quenched t_{yx} component, as shown in Figures 2C, D. In order to fully understand the polarization capability of our metastructure, the transmission spectra for device 1 with increased arm lengths of SRR are demonstrated in Figure 2E. It is found that the splitting window manifests a red-shift behavior, and the transmission of t_{xx} and t_{yx} slightly decreases. Then, we theoretically clarify the polarization response mechanism. Here, the twisted SRRs can be treated as two lumped *RLC* resonators having mutual inductance L_{12}. The excited currents can be expressed as [18, 39]

$$\frac{1}{C_1}\int i_1 dt + R_1 i_1 + L_1\frac{di_1}{dt} = L_{12}\frac{di_2}{dt} + gE_{in}, \tag{1}$$

$$\frac{1}{C_2}\int i_2 dt + R_2 i_2 + L_2\frac{di_2}{dt} = L_{12}\frac{di_1}{dt}, \tag{2}$$

where the subscripts "1" and "2" represent the left and right SRR, respectively, E_{in} is the electric field of the incident THz wave, and g is the gap dimension. Moreover, $C_1 = C_2 = C$, $R_1 = R_2 = R$, and $L_1 = L_2 = L$ are the capacitance, resistance, and inductance of twisted SRRs. We can derive the induced circulating currents as follows:

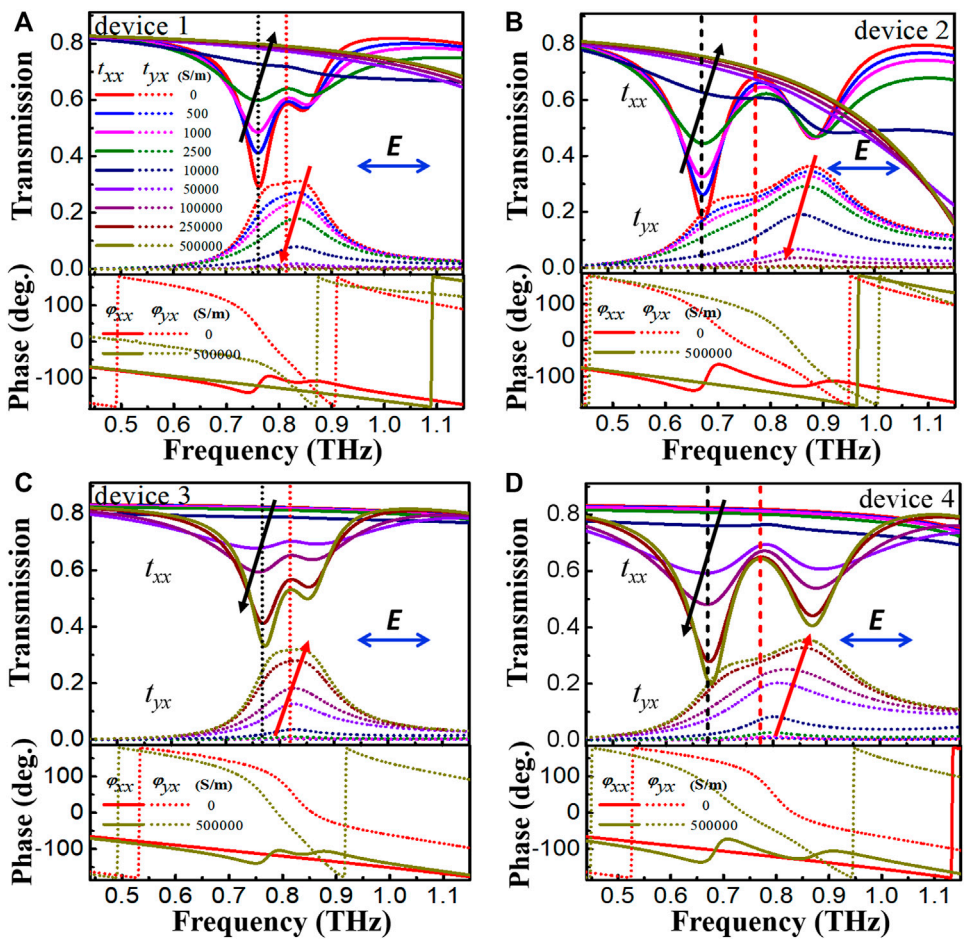

FIGURE 3
(A–D) Transmission responses of four hybrid metadevices for co-polarized and cross-polarized components with conductivities of the Si-bridge varying from 0 to 500,000 S/m. The bottom panels are the corresponding phase distributions at 0 and 500,000 S/m, respectively.

$$i_1(\omega) = gE_{in}\frac{\frac{1}{i\omega C} + R + i\omega L}{\left(\frac{1}{i\omega C} + R + i\omega L\right)^2 - (i\omega L_{12})^2}, \quad (3)$$

$$i_2(\omega) = gE_{in}\frac{i\omega L_{12}}{\left(\frac{1}{i\omega C} + R + i\omega L\right)^2 - (i\omega L_{12})^2}, \quad (4)$$

where ω is the angular frequency of the input THz wave. The excited electric dipoles can be deduced as $P_{1,2} \propto \int i_{1,2}dt = i_{1,2}/(-i\omega)$. Hence, the corresponding electric field formula is expressed by $E_{x,y} \propto d^2P_{1,2}/dt^2 = -\omega^2 P_{1,2}$, leading $\tilde{E}_x \propto \omega i_1$ and $\tilde{E}_y \propto \omega i_2$.

The curves of radiated field amplitude for the excited dipoles are calculated in Figure 2F. The radiation amplitude E_x results from the electric dipole directly excited by the incident THz wave at the left SRR. The E_y component comes from the electric dipole at the right SRR indirectly excited via the magnetic near-field coupling [18]. The theoretical amplitude responses are consistent with the aforementioned simulated transmission behaviors in Figure 2E, while the corresponding parameters are listed in Table 1. Therefore, we can conclude that the flat lineshape of t_{xx} in Figures 2C, D is caused by the breaking of the directly excited resonance mode with the introduction of a 4 μm gap in the bottom of the left SRR. The quenching of the cross-polarized t_{yx} component is ascribed to the annihilation of magnetic near-field coupling between the twisted SRRs.

3 Results and discussion

Moreover, realizing the reconfigurability of polarization converters is vital for the exploration of miniatured and multifunctional hybrid metadevices. In Figure 3A, we plot the transmission spectra for device 1 with different conductivities of the Si-bridge. When the conductivity is 0 S/m, the lineshapes of t_{xx} and t_{yx} are consistent with those in Figure 2A, which indicates that the Si-bridge acts as an insulator. Increasing the conductivity from 500 to 50,000 S/m, the transmission responses vary dramatically, accompanied by the annihilation of the t_{yx} component and resonance splitting window. These changes are due to that the Si-bridge with a high conductivity behaves like a metal to connect the top gap of the left SRR and weakens the LC mode, which suppresses the resonance coupling of two SRRs. In Figure 3B, the spectra of device 2 with a wider band show a similar evolution trend, but the resonance frequencies are different from those of device 1. These distinguishable resonance features especially marked

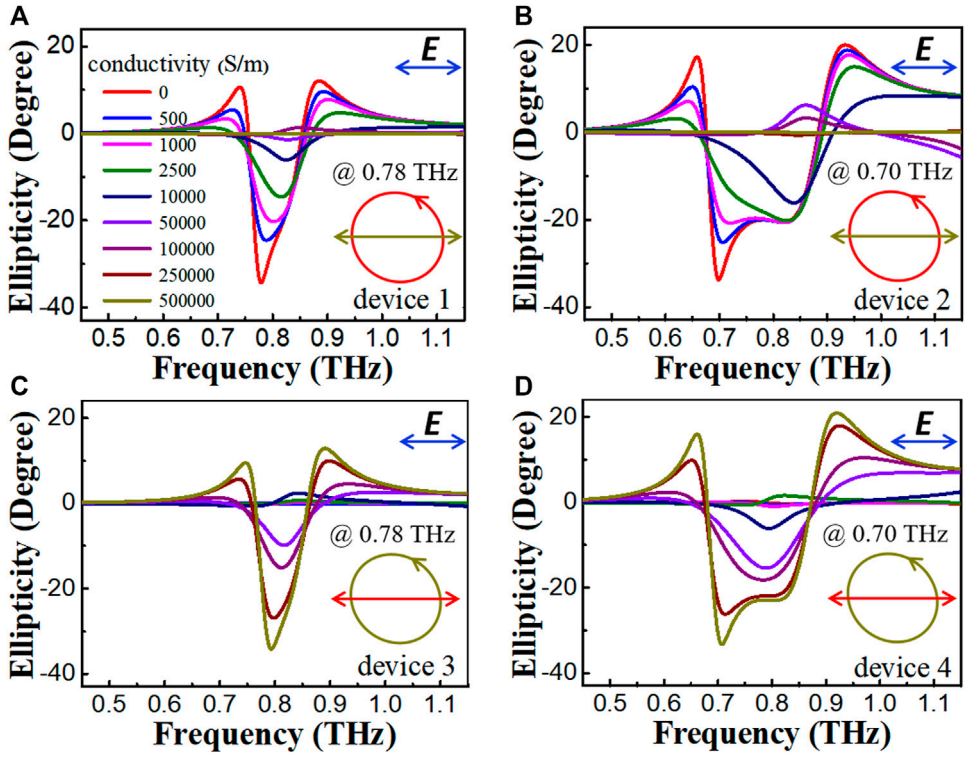

FIGURE 4
(A–D) Ellipticity of output polarization wave as a function of conductivities for four hybrid metadevices (insets: the switching of polarization states at given frequencies).

with two vertical dotted and dashed lines could provide more selective channels for multifunctional imaging applications that will be discussed later. The t_{yx} components and the resonance splitting windows of device 3 in Figure 3C gradually recover from the quenched state as the conductivity increases. This recovery arises from the reconstruction of the resonance coupling between two SRRs when the Si-bridge has a higher conductivity. It is noticeable that the tunable reappearance of the cross-polarized component for device 3 corresponds to an inverse evolution process in device 1. As can be seen in Figures 3B, D, the inverse behaviors of the polarization conversion also exist in device 2 and device 4. We can deduce that the inverse and full modulation of the cross-polarized components can be achieved by tuning the conductivity of the Si-bridge. The corresponding phase distributions φ_{xx} for t_{xx} and φ_{yx} for t_{yx} components with the conductivity of the Si-bridge at 0 and 500,000 S/m are depicted in the bottom panels.

It is known that the polarization state of the output light can be modulated by the amplitude ratio and phase lag between the co- and the cross-polarized components. Hence, we introduce four Stokes parameters [8] to numerically elucidate the output states of the THz wave. Those parameters are $S_0 = |\tilde{t}_{xx}|^2 + |\tilde{t}_{yx}|^2$, $S_1 = |\tilde{t}_{xx}|^2 - |\tilde{t}_{yx}|^2$, $S_2 = 2|\tilde{t}_{xx}||\tilde{t}_{yx}|\cos\varphi_{diff}$, and $S_3 = 2|\tilde{t}_{xx}||\tilde{t}_{yx}|\sin\varphi_{diff}$, where φ_{diff} is the phase difference ($\varphi_{diff} = \varphi_{xx} - \varphi_{yx}$). Then, we can calculate $\tan 2\alpha = S_2/S_1$ and $\tan 2\chi = S_3/S_0$, where α and χ represent the polarization azimuth angle and ellipticity, respectively. Here, $-45^\circ \leq \chi \leq 45^\circ$ represents the elliptically (0° for linear polarization, 45° for a perfect RCP, and -45° for a perfect LCP) polarized state. We plot the ellipticity spectra with the x-polarized incidence in Figure 4. When the conductivity of the Si-bridge is 0 S/m, the ellipticity of device 1 is -35° at 0.78 THz. This value tends to be 0° as the conductivity increases. Combined with α and χ, the corresponding polarization states for 0 S/m and 500,000 S/m are shown in the inset of Figure 4A, clearly showing a conversion from an LCP to an LP wave. Similarly, there is also a significant ellipticity modulation for device 2 from -34°–0° at 0.70 THz in Figure 4B. The calculated results reveal that device 1 and device 2 could work as tunable polarizers like the quarter wave plates. On the contrary, as demonstrated in Figures 4C, D, the ellipticity is tailored from 0° to -35° at 0.78 THz for device 3 and from 0° to -34° at 0.70 THz for device 4. Thus, device 3 and device 4 are capable of converting an LP wave to LCP light with increased conductivity of the Si-bridge.

Considering the anisotropic properties of our twisted SRR metadevices, we further study the transmission responses for device 2 and device 4 with the y-polarized incident THz wave. At the Si-bridge conductivity of 0 S/m, the red lines in Figure 5A exhibit that the polarization conversion capability and resonance splitting window of device 2 are still retained. As the conductivity increases to 2500 S/m, the co-polarized t_{yy} component decreases and is accompanied by the gradual disappearance of the splitting window. From 10,000 S/m to 500,000 S/m, the t_{xy} component is quenched. These phenomena stem from the suppression of resonance coupling between two SRRs. Different from the x-polarized incidence, the co-polarized spectra at the higher conductivity only have an apparent dip induced by LC resonance, which is confirmed by the simulated circular current

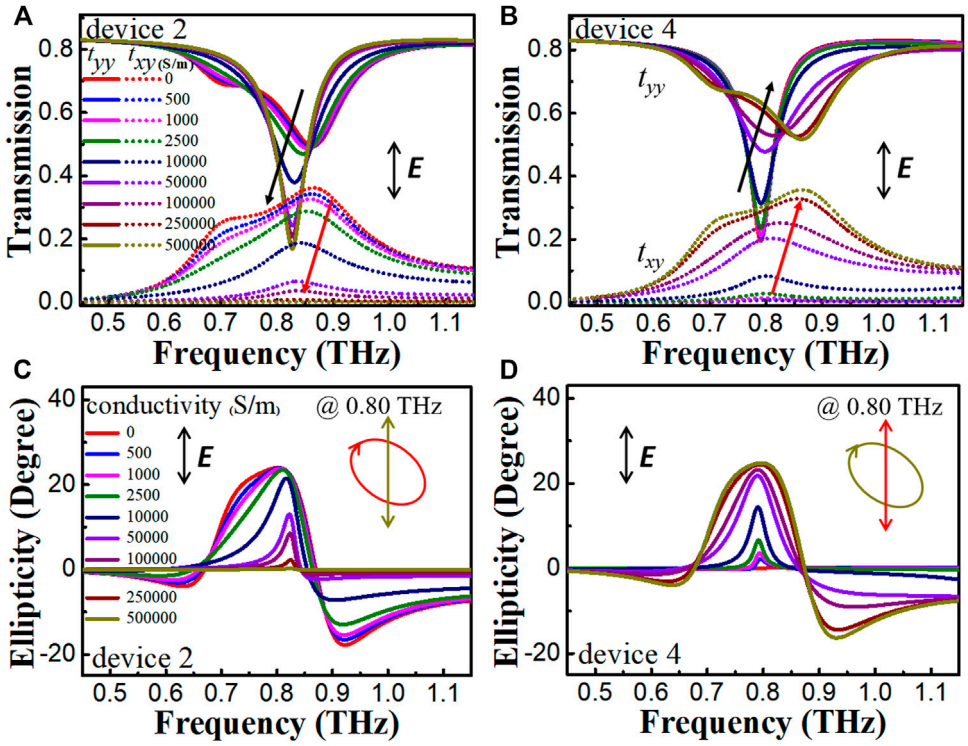

FIGURE 5
Simulated co- and cross-polarized transmission spectra for hybrid metadevices based on **(A)** device 2 and **(B)** device 4 against conductivities of the Si-bridge with the *y*-polarized incident THz wave. **(C, D)** The corresponding ellipticity of output polarization wave.

and highly concentrated electric field around the right gap (not shown). Intriguingly, the cross-polarized components in Figures 5A, B and their evolution process are completely identical. Furthermore, the transmission evolution of device 4 in Figure 5B is also an inverse process compared to device 2, which fully indicates that even after adjusting the polarized direction of the incident THz wave, our metadevice can still work as an inverse and controllable polarizer. As shown in Figures 5C, D, we calculate the ellipticity curves based on Stokes parameters. The ellipticity is from 27° to 0° at 0.80 THz for device 2 with the increased conductivity. These modulation results confirm that these devices could realize the conversion from an RCP wave to LP light. Under the same operating frequency, device 4 achieves conversion from an LP state to RCP wave. The aforementioned reconfigurable polarization states are shown in the insets. Combined with these observations, we can conclude that our metadevices possess the ability to convert LP light into LCP or RCP waves, as well as LCP or RCP into LP states.

To broaden the multi-scenario application, especially in the THz imaging, with the obtained polarization characteristics, we design the H-shape and pentagram target patterns composed of mutually perpendicular metallic gratings, as shown in Figures 6A, B. The width of the Au wire is 2 μm, and its duty ratio is 1:1. It is known that the THz waves with the polarized direction perpendicular to the grating could pass through the structure, while the waves with the parallel polarized direction were reflected [15]. Hence, the left target grating could permit transmission of the t_{xx} component and hinder the transmission of the t_{yx} component. The right part has the opposite properties. So, the active control of t_{xx} and t_{yx} components lays the foundation for dynamical imaging of the target patterns. Here, we select two representative frequencies of 0.76 and 0.82 THz marked by the black and red dotted lines in Figure 3A for device 1 to demonstrate the imaging function, as shown in Figure 6C. At the conductivity of 0 S/m, the transmission at the marked frequencies has a minimum value of t_{xx} and a maximum value of t_{yx}. As the conductivity is 500,000 S/m, the t_{xx} value is the largest, and the t_{yx} value is reduced to 0. Specifically, the higher transmission values correspond to the higher visibility of these target images. Therefore, the visibility of the left half of the H-shape imaged by device 1 at 0.76 THz gradually becomes clear, while the right half becomes blurry and finally invisible at 100,000 S/m. The erasure conductivity at 0.82 THz needs to increase to 500,000 S/m, which shows the frequency-dependent imaging modulation susceptibility. Figure 6D exhibits similar imaging properties for pentagram targets at the selected frequencies of 0.68 and 0.78 THz indicated in Figure 3B for device 2. According to the inverse evolution process between the transmission curves in Figures 3A, C, the imaging in Figure 6E for device 3 also shows the inverse evolution feature compared to Figures 6C, 6D, F. Thus, this amplitude-based imaging depends on frequency selection. It can be seen that the tunable co- and cross-polarized amplitude components can empower the indirect imaging of target patterns, which is one strategy in meta-based imaging.

Actually, phase as an important physical quantity can provide valuable information. Hence, combined with amplitude and phase, we propose a novel approach to illustrate the ellipticity-dependent direct imaging, as shown in Figure 7. Two planar arrays are designed

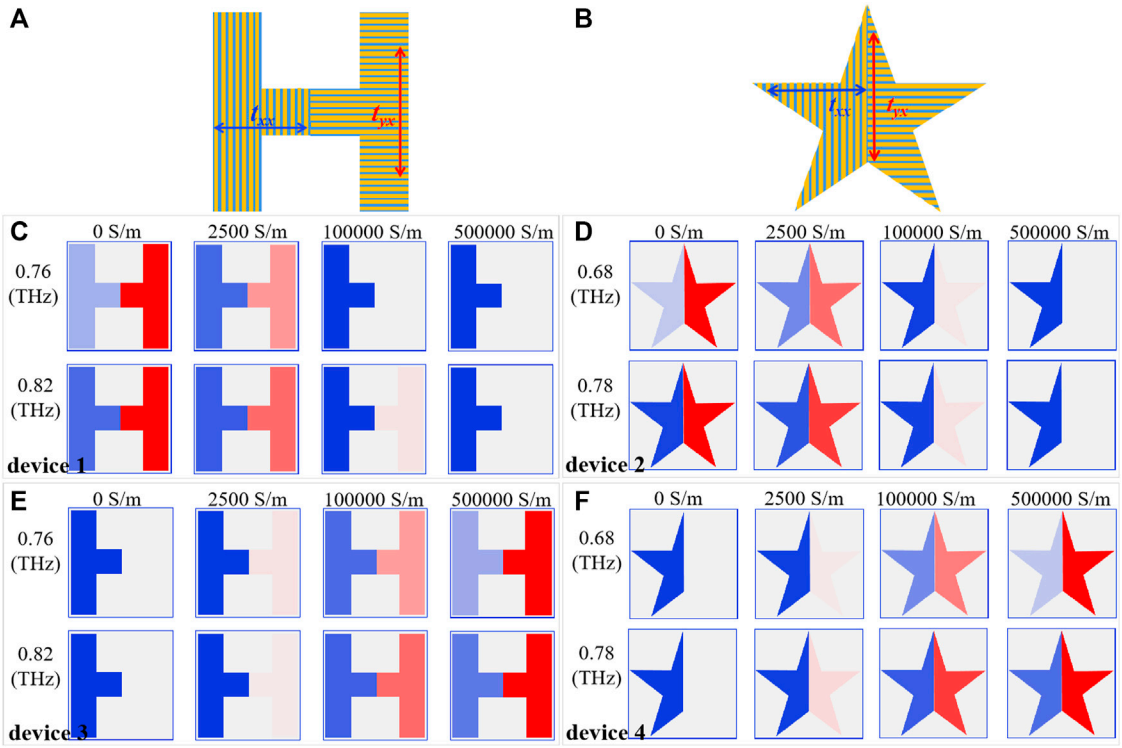

FIGURE 6
(A, B) Schematics of the designed patterns H shape and pentagram for polarization-dependent imaging. **(C–F)** The visibility evolution of the target patterns at given frequencies with different conductivities of the Si-bridge.

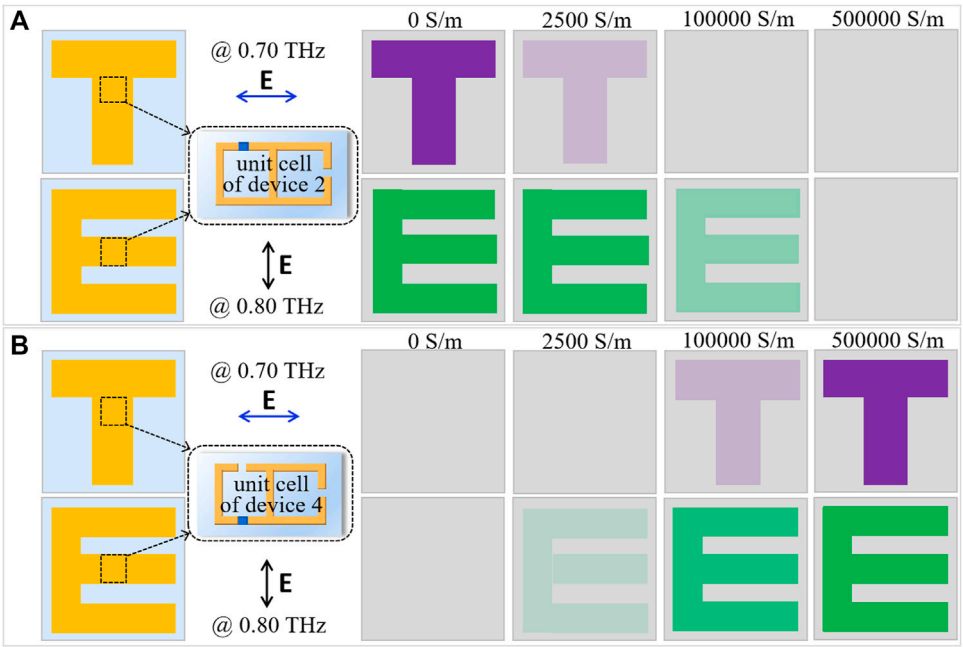

FIGURE 7
Schematics of the T shape and E shape composed of the unit cells of device 2 and device 4 for active ellipticity-dependent imaging. **(A, B)** The imaging process of the target patterns with the *x*-polarized and *y*-polarized incident THz waves at given frequencies by varying the conductivity of the Si-bridge.

to construct T- and E-shape, where the regions with letters are composed of metastructure. For instance, in Figure 7A, with the structure of device 2, according to the calculated maximum ellipticity in Figures 4B, 5B, at 0.7 THz, the T-shape is clearly imaged and becomes invisible at 100,000 S/m under the *x*-polarized incident THz wave. With the *y*-polarized incidence, at 0.8 THz, the E-shape is invisible when the conductivity is 500,000 S/m. Apparently, the imaging susceptibility based on device 2 under the *x*-polarized incidence is more vulnerable than that under the *y*-polarized incidence. As can be seen from Figure 7B, if those target regions are replaced by the structure of device 4, the imaging process exhibits the inverse evolution trend. Specifically, the E-shape appears at 2500 S/m, but this appearance of the T-shape occurs at 100,000 S/m, showing that the former exhibits the larger sensitivity to the *y*-polarized incidence. It is worth emphasizing that the ellipticity-dependent direct imaging is operated based on the amplitude–phase synergistic effect, which facilitates encryption imaging and information security.

As we know, polarization conversion efficiency is an important index to assess the performance of polarizers. To improve this efficiency, some research studies have involved the use of all-dielectric metamaterials or reflective metadevices [25, 30]. In addition, the introduction of two-layer orthogonal metallic gratings having the Fabry–Perot cavity in our metadevice is also an effective method, which is verified by our further numerical simulations (not shown).

4 Conclusion

In summary, we demonstrated a hybrid twisted SRR metadevice with polarization conversion capability and clarified the response mechanism using a coupled resonator model. Combined with the photosensitive conductivity of the Si-bridge, the inverse and reconfigurable modulation of the cross-polarized component can be implemented. The results indicate that our metadevices can function as tunable linear-to-circular and circular-to-linear polarizers. Based on these inverse polarization switching performances, amplitude-dependent indirect imaging and amplitude-phase synergistic imaging can be achieved. Our proposed hybrid metadevices can not only realize the switching of multiple polarization states of the THz wave but also exhibit great application potential in the development of future encryption imaging and information security in the THz regime.

Data availability statement

The original contributions presented in the study are included in the article/Supplementary Material; further inquiries can be directed to the corresponding author.

Author contributions

YD wrote the initial manuscript, made the graph, and performed the calculation. QZ, CZ, TN, and YS obtained funding and designed and reviewed the manuscript. XZ, PZ, and WL contributed sections of the initial drafts. All authors contributed to the article and approved the submitted version.

Funding

This study was funded by the National Natural Science Foundation of China (62075142, 12174228, and 12174272).

Conflict of interest

The authors declare that the research was conducted in the absence of any commercial or financial relationships that could be construed as a potential conflict of interest.

Publisher's note

All claims expressed in this article are solely those of the authors and do not necessarily represent those of their affiliated organizations, or those of the publisher, the editors, and the reviewers. Any product that may be evaluated in this article, or claim that may be made by its manufacturer, is not guaranteed or endorsed by the publisher.

References

1. Smith DR, Pendry JB, Wiltshire MCK. Metamaterials and negative refractive index. *Science* (2004) 305(5685):788–92. doi:10.1126/science.1096796

2. Landy N, Sajuyigbe S, Mock J, Smith D, Padilla W. Perfect metamaterial absorber. *Phys Rev Lett* (2008) 100(20):207402. doi:10.1103/PhysRevLett.100.207402

3. Yu N, Genevet P, Kats MA, Aieta F, Tetienne J-P, Capasso F, et al. Light propagation with phase discontinuities: Generalized laws of reflection and refraction. *Science* (2011) 334(6054):333–7. doi:10.1126/science.1210713

4. Zheludev NI, Kivshar YS. From metamaterials to metadevices. *Nat Mater* (2012) 11(11):917–24. doi:10.1038/NMAT3431

5. Balci O, Kakenov N, Karademir E, Balci S, Cakmakyapan S, Polat EO, et al. Electrically switchable metadevices via graphene. *Sci Adv* (2018) 4(1):eaao1749. doi:10.1126/sciadv.aao1749

6. Hu Y, Jiang T, Zhou J, Hao H, Sun H, Ouyang H, et al. Ultrafast terahertz frequency and phase tuning by all-optical molecularization of metasurfaces. *Adv Opt Mater* (2019) 7(22):1901050. doi:10.1002/adom.201901050

7. Jung H, Koo J, Heo E, Cho B, In C, Lee W, et al. Electrically controllable molecularization of terahertz meta-atoms. *Adv Mater* (2018) 30(31):1802760. doi:10.1002/adma.201802760

8. Cong L, Srivastava YK, Singh R. Near-field inductive coupling induced polarization control in metasurfaces. *Adv Opt Mater* (2016) 4(6):848–52. doi:10.1002/adom.201500681

9. Zhao X, Boussaid F, Bermak A, Chigrinov VG. High-resolution thin "guest-host" micropolarizer arrays for visible imaging polarimetry. *Opt Express* (2011) 19(6):5565–73. doi:10.1364/OE.19.005565

10. Guan S, Cheng J, Chen T, Chang S. Widely tunable polarization conversion in low-doped graphene-dielectric metasurfaces based on phase compensation. *Opt Lett* (2020) 45(7):1742–5. doi:10.1364/OL.385159

11. Pu M, Chen P, Wang Y, Zhao Z, Huang C, Wang C, et al. Anisotropic meta-mirror for achromatic electromagnetic polarization manipulation. *Appl Phys Lett* (2013) 102(13):131906. doi:10.1063/1.4799162

12. Guo Y, Wang Y, Pu M, Zhao Z, Wu X, Ma X, et al. Dispersion management of anisotropic metamirror for super-octave bandwidth polarization conversion. *Sci Rep* (2015) 5:8434. doi:10.1038/srep08434

13. Li JT, Wang GC, Yue Z, Liu JY, Li J, Zheng C, et al. Dynamic phase assembled terahertz metalens for reversible conversion between linear polarization and arbitrary circular polarization. *Opto-Electronic Adv* (2022) 5(1):210062. doi:10.29026/oea.2022.210062

14. Yamada I, Takano K, Hangyo M, Saito M, Watanabe W. Terahertz wire-grid polarizers with micrometer-pitch Al gratings. *Opt Lett* (2009) 34(3):274–6. doi:10.1364/OL.34.000274

15. Cong L, Cao W, Zhang X, Tian Z, Gu J, Singh R, et al. A perfect metamaterial polarization rotator. *Appl Phys Lett* (2013) 103(17):171107. doi:10.1063/1.4826536

16. Kim T-T, Oh S, Kim H-D, Park H, Hess O, Min B, et al. Electrical access to critical coupling of circularly polarized waves in graphene chiral metamaterials. *Sci Adv* (2017) 3(9):e1701377. doi:10.1126/sciadv.1701377

17. Arbabi A, Horie Y, Bagheri M, Faraon A. Dielectric metasurfaces for complete control of phase and polarization with subwavelength spatial resolution and high transmission. *Nat Nanotechnol* (2015) 10(11):937–43. doi:10.1038/NNANO.2015.186

18. Li C, Chang C-C, Zhou Q, Zhang C, Chen H-T. Resonance coupling and polarization conversion in terahertz metasurfaces with twisted split-ring resonator pairs. *Opt Express* (2017) 25(21):25842–52. doi:10.1364/OE.25.025842

19. Hu S, Yang S, Liu Z, Li J, Gu C. Broadband cross-polarization conversion by symmetry-breaking ultrathin metasurfaces. *Appl Phys Lett* (2017) 111(24):241108. doi:10.1063/1.5006540

20. Chen D, Yang J, Huang J, Bai W, Zhang J, Zhang Z, et al. The novel graphene metasurfaces based on split-ring resonators for tunable polarization switching and beam steering at terahertz frequencies. *Carbon* (2019) 154:350–6. doi:10.1016/j.carbon.2019.08.020

21. Zheng G, Mühlenbernd H, Kenney M, Li G, Zentgraf T, Zhang S. Metasurface holograms reaching 80% efficiency. *Nat Nanotechnol* (2015) 10(4):308–12. doi:10.1038/NNANO.2015.2

22. Wen D, Yue F, Li G, Zheng G, Chan K, Chen S, et al. Helicity multiplexed broadband metasurface holograms. *Nat Commun* (2015) 6:8241. doi:10.1038/ncomms9241

23. Khorasaninejad M, Zhu W, Crozier K. Efficient polarization beam splitter pixels based on a dielectric metasurface. *Optica* (2015) 2(4):376–82. doi:10.1364/OPTICA.2.000376

24. Cong L, Xu N, Han J, Zhang W, Singh R. Emergent functionality and controllability in few-layer metasurfaces. *Adv Mater* (2015) 27(36):5410–21. doi:10.1002/adma.201501506

25. Zang X, Ding H, Intaravanne Y, Chen L, Peng Y, Xie J, et al. A multi-foci metalens with polarization-rotated focal points. *Laser Photon Rev* (2019) 13(12):1900182. doi:10.1002/lpor.201900182

26. Wang P, Hu R, Huang X, Wang T, Hu S, Hu M, et al. Terahertz chiral metamaterials enabled by textile manufacturing. *Adv Mater* (2022) 34(16):2110590. doi:10.1002/adma.202110590

27. Pendry JB, Holden AJ, Robbins DJ, Stewart WJ. Magnetism from conductors and enhanced nonlinear phenomena. *IEEE Trans Microwave Theor Tech* (1999) 47(11):2075–84. doi:10.1109/22.798002

28. Marqués R, Medina F, Rafii-El-Idrissi R. Role of bianisotropy in negative permeability and left-handed metamaterials. *Phys Rev B* (2002) 65(14):144440. doi:10.1103/PhysRevB.65.144440

29. Khatua S, Chang WS, Swanglap P, Olson J, Link S. Active modulation of nanorod plasmons. *Nano Lett* (2011) 11(9):3797–802. doi:10.1021/nl201876r

30. Zhang Y, Feng Y, Zhao J. Graphene-enabled tunable multifunctional metamaterial for dynamical polarization manipulation of broadband terahertz wave. *Carbon* (2020) 163:244–52. doi:10.1016/j.carbon.2020.03.001

31. Isozaki A, Kanda N, Nemoto N, Konishi K, Takahashi H, Kuwata-Gonokami M, et al. Enantiomeric switching of chiral metamaterial for terahertz polarization modulation employing vertically deformable MEMS spirals. *Nat Commun* (2015) 6:8422. doi:10.1038/ncomms9422

32. Zhang Y, Feng Y, Jiang T, Cao J, Zhao J, Zhu B. Tunable broadband polarization rotator in terahertz frequency based on graphene metamaterial. *Carbon* (2018) 133:170–5. doi:10.1016/j.carbon.2018.03.038

33. Song Z, Zhang J. Achieving broadband absorption and polarization conversion with a vanadium dioxide metasurface in the same terahertz frequencies. *Opt Express* (2020) 28(8):12487–97. doi:10.1364/OE.391066

34. Li J, Li X. Switchable tri-function terahertz metasurface based on polarization vanadium dioxide and photosensitive silicon. *Opt Express* (2022) 30(8):12823–34. doi:10.1364/OE.454240

35. Cong L, Srivastava YK, Zhang H, Zhang X, Han J, Singh R. All-optical active THz metasurfaces for ultrafast polarization switching and dynamic beam splitting. *Light-sci Appl* (2018) 7:228–36. doi:10.1038/s41377-018-0024-y

36. Hu Y, Tong M, Hu S, He W, Cheng X, Jiang T. Reassessing Fano resonance for broadband high-efficiency, and ultrafast terahertz wave switching. *Adv Sci* (2023) 10:2204494. doi:10.1002/advs.202204494

37. Hu Y, Jiang T, Sun H, Tong M, You J, Zheng X, et al. Ultrafast frequency shift of electromagnetically induced transparency in terahertz metaphotonic devices. *Laser Photon Rev* (2020) 14(3):1900338. doi:10.1002/lpor.201900338

38. Deng Y, Zhou Q, Zhang P, Jiang N, Ning T, Liang W, et al. Heterointerface-enhanced ultrafast optical switching via manipulating metamaterial-induced transparency in a hybrid terahertz graphene metamaterial. *ACS Appl Mater Inter* (2021) 13(11):13565–75. doi:10.1021/acsami.0c22862

39. Zhao X, Fan K, Zhang J, Keiser GR, Duan G, Averitt RD, et al. Voltage-tunable dual-layer terahertz metamaterials. *Microsyst Nanoeng* (2016) 2:16025. doi:10.1038/micronano.2016.25